Title

Supersonic transient magnetic resonance elastography for quantitative assessment of tissue elasticity

Journal

Physics in Medicine and Biology, 62(10)

ISSN

0031-9155

Authors

Liu, Yu
Liu, Jingfei
Fite, Brett Z
et al.

Publication Date

2017-05-21

DOI

10.1088/1361-6560/aa6674

Peer reviewed

HHS Public Access

Author manuscript

Phys Med Biol. Author manuscript; available in PMC 2018 May 21.

Published in final edited form as:

Phys Med Biol. 2017 May 21; 62(10): 4083–4106. doi:10.1088/1361-6560/aa6674.

Supersonic transient magnetic resonance elastography for quantitative assessment of tissue elasticity

Yu Liu[1,4], **Jingfei Liu**[1,4], **Brett Z Fite**[1], **Josquin Foiret**[1], **Asaf Ilovitsh**[1], **J Kent Leach**[1], **Erik Dumont**[2], **Charles F Caskey**[3], and **Katherine W Ferrara**[1,4,5]

[1]Department of Biomedical Engineering, University of California, Davis, CA 95616, United States of America

[2]Image Guided Therapy, Pessac, France

[3]VUIIS, Vanderbilt University, Nashville, TN, United States of America

Abstract

Non-invasive, quantitative methods to assess the properties of biological tissues are needed for many therapeutic and tissue engineering applications. Magnetic resonance elastography (MRE) has historically relied on external vibration to generate periodic shear waves. In order to focally assess a biomaterial or to monitor the response to ablative therapy, the interrogation of a specific region of interest by a focused beam is desirable and transient MRE (t-MRE) techniques have previously been developed to accomplish this goal. Also, strategies employing a series of discrete ultrasound pulses directed to increasing depths along a single line-of-sight have been designed to generate a quasi-planar shear wave. Such 'supersonic' excitations have been applied for ultrasound elasticity measurements. The resulting shear wave is higher in amplitude than that generated from a single excitation and the properties of the media are simply visualized and quantified due to the quasiplanar wave geometry and the opportunity to generate the wave at the site of interest. Here for the first time, we extend the application of supersonic methods by developing a protocol for supersonic transient magnetic resonance elastography (sst-MRE) using an MR-guided focused ultrasound system capable of therapeutic ablation. We apply the new protocol to quantify tissue elasticity *in vitro* using biologically-relevant inclusions and tissue-mimicking phantoms, compare the results with elasticity maps acquired with ultrasound shear wave elasticity imaging (US-SWEI), and validate both methods with mechanical testing. We found that a modified time-of-flight (TOF) method efficiently quantified shear modulus from sst-MRE data, and both the TOF and local inversion methods result in similar maps based on US-SWEI. With a three-pulse excitation, the proposed sst-MRE protocol was capable of visualizing quasi-planar shear waves propagating away from the excitation location and detecting differences in shear modulus of 1 kPa. The techniques demonstrated here have potential application in real-time *in vivo* lesion detection and monitoring, with particular significance for image-guided interventions.

[5]Author to whom any correspondence should be addressed: kwferrara@ucdavis.edu.

[4]These authors contributed equally to this paper.

Keywords

supersonic ultrasound; elastography; MR-guided ablation; time of flight; cancer

1. Introduction

Palpation, a time-tested diagnostic tool, has been used to differentiate between normal and abnormal tissues based on differences in mechanical properties in varied physiological and pathological states (Duck 1990, Sarvazyan *et al* 1995, Barton *et al* 1999). However, palpation is applicable only to superficial organs and is qualitatively and subjectively limited to the sensitivity of the practitioner. Therefore, methods to quantitatively and non-invasively assess the mechanical properties of tissue have become popular. Elastographic techniques generate a mechanical disturbance in tissue and use ultrasound (US) or magnetic resonance (MR) imaging of the propagation of the disturbance to map tissue properties and produce anatomical images for comparison (Plewes *et al* 2000, Aguilo *et al* 2010, Bamber *et al* 2013, Cosgrove *et al* 2013). Elastographic imaging has been reported to differentiate malignant and benign lesions in the liver (Cho *et al* 2010, Bavu *et al* 2011, Chen *et al* 2013), breast (Garra *et al* 1997, Plewes *et al* 2000, Itoh *et al* 2006, Zhi *et al* 2007, Cosgrove *et al* 2013) and prostate (Tsutsumi *et al* 2007, Salomon *et al* 2008, Sarvazyan *et al* 2011, Walz *et al* 2011, Cosgrove *et al* 2013, Brock *et al* 2013), and to detect pathological changes in lymph nodes (Janssen *et al* 2007, Lyshchik *et al* 2007, Giovannini *et al* 2009, Choi *et al* 2011, Cosgrove *et al* 2013) and pre-malignant parenchymal changes in the liver, such as hepatic cirrhosis and fibrosis (Yeh *et al* 2002, Sandrin *et al* 2003, Friedrich-Rust *et al* 2008, Kirk *et al* 2009, Friedman 2010).

In contrast to the longitudinal waves used by ultrasound imaging, the application of a mechanical perturbation in tissue generates shear waves in which the particle displacement is perpendicular to the direction of wave propagation. These shear waves propagate at a relatively low velocity in soft tissue (a few m s^{-1}) and can be imaged; however, imaging of their propagation is limited by attenuation and reflections at interfaces between tissues with differing material properties. Using ultrasound imaging to assess tissue stiffness, early work relied on quasi-static forces applied externally (compression) to interrogate tissue stiffness (Ophir *et al* 1991, Cespedes *et al* 1993, Kallel and Bertrand 1996). Harmonic excitation with frequencies from 20 to several hundred Hertz was then applied to drive soft tissue using a mechanical vibrator (Lerner *et al* 1990).

Alternatively, mapping tissue stiffness deep within the body has been accomplished by using a focused sound beam where acoustic radiation force (ARF) creates the localized displacement and the resulting shear wave (Sarvazyan *et al* 1998, Wu *et al* 2000, Nightingale *et al* 2002, Lizzi *et al* 2003, Souchon *et al* 2008). By creating the displacement with a focused transducer, the radiation force is greatly reduced outside of the focal zone and therefore tissue properties can be assessed in a user-selected region of interest. ARF impulse (ARFI)-induced shear wave imaging has been implemented on commercial diagnostic ultrasound scanners and applied in human studies (Palmeri *et al* 2008). The ARF excitation can be transient, as applied here, or harmonic (Urban *et al* 2011, Konofagou *et al* 2012).

An ultrasound-based supersonic shear wave elasticity imaging (US-SWEI) approach has previously been proposed for use with ultrasound tracking. In this mode, a train of pulses is rapidly transmitted and the focal depth changed in real time between transmissions (Bercoff *et al* 2004c). As a result, quasi-planar shear waves are generated and the source of these waves can be directed to the region of interest. In the previous implementations, the resulting shear waves were imaged by an ultrafast, ultrasonic scanner. This technique has been investigated for breast cancer diagnosis where soft fatty tissues (Young's modulus (E), from 5 to 10 kPa) were differentiated from breast parenchyma ($E \sim 30$ kPa) and malignant lesions ($E > 100$ kPa) (Tanter *et al* 2008). Here, for the first time we combine supersonic excitation with MR imaging.

MR elastography (MRE) was first introduced in 1995, where an external vibration was used to generate periodic shear waves that were detected by MRI. Based on the shear wave speed, the stiffness of the tissue was reconstructed (Muthupillai *et al* 1995, Muthupillai *et al* 1996). MRI can also be used to provide a three-dimensional (3D) view of anatomy during interventions and does not introduce speckle into the images of displacement. The shear motion is encoded into the MR phase images by adding motion encoding gradients (MEGs) into conventional MR pulse sequences (Sarvazyan *et al* 1998, Souchon *et al* 2008). Traditional MRE has used an external mechanical vibrator to generate shear waves (Muthupillai *et al* 1995, Muthupillai *et al* 1996). While vibrator-based MRE can be applied in many scenarios, the ability to directly interrogate the elasticity of the treated region is desirable for interventional applications. The method developed here is ideal for such applications as the ultrasound beam can be immediately directed to the ablated region without moving the patient or transducer. We have previously demonstrated real-time thermometry and performed ablative procedures using this system (Fite *et al* 2012, Wong *et al* 2016).

ARF has also been used in MR-elastography, using a modified gradient echo sequence to monitor transient shear wave propagation by varying the delay time between ultrasound excitation and MEG. Such methods of transient MRE (t-MRE) have been tested in biological tissues *ex vivo* and *in vivo* (McCracken *et al* 2005, Souchon *et al* 2008). We have previously combined MR-ARFI and shear wave imaging within a single sequence (Liu *et al* 2015). Displacement and shear wave velocity estimates were obtained with the same acquisition and used to detect changes in tissue properties resulting from thermal therapy. However, with this protocol, shear wave propagation estimates were limited by the required timing of the ultrasound pulse and time between MEGs.

Our ultimate goal is to develop a supersonic technique to detect changes in tissue properties following magnetic resonance-guided focused ultrasound (MRgFUS) ablation. In this scenario, the location of the lesion to be treated is known and the same transducer is used both to ablate tissue and to assess the changes in tissue properties. There is a tremendous opportunity to immediately assess the impact of treatment by using the same transducer and amplifiers. The design constraints for an MRgFUS ablative system are quite different from a pulser used in US imaging and present different challenges than those relevant to t-MRE. The MRgFUS design is driven by the need to minimize RF interference with the MR imaging, by the high and continuous-wave power output required and by the requirement for

the transducer to be as efficient as possible (for thermal ablation). The MRgFUS generator is therefore designed to produce long, spectrally pure RF pulses and the transducer is narrow band to improve efficiency. There are therefore no fundamental limitations but rather design choices in the MRgFUS system that introduce technical limitations in the generation of fast, very short, beam steered, pulses. The additional design aspects related to imaging changes in tissue properties result from the opportunity to excite the shear wave within or adjacent to the lesion before and after ablation. The goal is to detect and approximately map changes in tissue properties immediately surrounding this region. By exciting the shear wave locally, the propagation of the shear wave need only be tracked over a very short distance (approximately the size of the inclusion), the MR echo time can be minimized (and therefore the signal-to-noise ratio enhanced) and reflections from the far boundaries of the lesion do not substantively interfere with the acquisition.

We have therefore developed the supersonic transient MRE (sst-MRE) approach described here to combine the desirable features of t-MRE with the high signal-to-noise ratio obtained with supersonic excitation. The focus of the ultrasound beam is updated in real-time during the MR image acquisition; however, the rate of update is limited due to the narrowband and low noise design characteristics. For the sst-MRE measurements obtained with our system, the sampling interval in the time domain is relatively large (0.45 ms) compared with that of US-SWEI data (0.1 ms). With this limited sampling, a processing method based on the time of flight (TOF) method (McLaughlin and Renzi 2006a, 2006b, Palmeri *et al* 2008) was developed. The method applied here relies on identifying the peak displacement in the spatial domain, rather than in the time domain (as implemented in the previous TOF method), and interpolating the resulting spatial map of shear modulus. The sst-MRE approach is compared with US-SWEI images processed with both the TOF method and with a local inversion method (LIM) based on the simplified, linear wave equation and previously implemented in US-SWEI for reconstructing soft tissue elasticity maps (Bercoff *et al* 2004a, 2004c). While we design these methods for interventional MR-guided applications, the techniques introduced here also have application in the assessment of biomaterials where known inhomogeneities are characterized.

2. Materials and methods

2.1. Tissue-mimicking phantom preparation

Gelatin (Sigma Co., St. Louis, USA) and agar (Alfa Aesar, MA, USA) were used in this study to fabricate tissue-mimicking phantoms (table 1). These phantoms possess Young's moduli that span a range from below 15 kPa to ~90 kPa, a clinically relevant range of normal and malignant breast tissues as reported by Tanter *et al* (2008). Scatterers were added into the hydrogel phantoms to provide the recommended backscatter coefficient to mimic the internal structure of soft tissues and generate speckle patterns in ultrasound images. As suggested by Bude and Adler (1995), 2% Psyllium hydrophilic mucilloid fiber (sugar-free Metamucil®) was added into the phantoms to form echogenic media and creates an attenuation coefficient of 0.40 dB cm^{-1} MHz^{-1}. 0.01% Gadolinium was also added in the solution in order to improve the signal-to-noise ratio (SNR) for MRI.

The tissue-mimicking phantoms were prepared according to a previous report with minor modifications (Liu *et al* 2015). Briefly, the components in table 1 were mixed with deionized water at ambient temperature and heated until all powder was dissolved. The degassed solution was then poured into a mold and cooled until firm. In order to produce internal inclusions, a layer of the degassed mixture was first cooled and congealed. Inclusions (such as excised tumors and agar cubes ($7 \times 7 \times 7$ mm^3)) were then placed on the top of the first layer, covered by the remainder of the solution and allowed to congeal. The compositions of the phantoms investigated in this study are summarized in table 1.

2.2. MR-based transient shear wave elasticity imaging

2.2.1. MR-guided focused ultrasound system—sst-MRE was performed on an MRgFUS system, consisting of a 7T MR scanner (Biospec 70/30 USR, Bruker Biospin, Germany), a MR-compatible 16-element annular array transducer (IMASONIC SAS, France) and an MR-compatible 3D positioning and high intensity pulser system (Lab FUS, Image Guided Therapy (IGT), France) capable of generating more than 100 acoustic Watts (Fite *et al* 2012). A circularly polarized radiofrequency coil with an internal diameter of 154 mm (Bruker Biospin, Germany) was used for both transmission and reception. The annular ultrasound array has a central frequency of 3 MHz, a diameter of 48 mm, a radius of curvature of 35 mm, and a −6 dB focal volume of $0.5 \times 0.5 \times 2$ mm^3.

2.2.2. sst-MRE protocol—MR images were acquired using a modified two-dimensional (2D) spin-echo imaging sequence (figure 1(a)), where a pair of inverted bipolar MEGs was programmed into the sequence and used to convert the local displacement into a phase shift. The supersonic train of ultrasound pulses began at a variable time, t_d, before the MEGs. The ultrasound beam was oriented vertically (figure 1(a)) and the generated shear wave (approximately cylindrical in shape) propagated horizontally. The MEG was programmed to encode motion along the direction of ultrasound propagation (perpendicular to the shear wave propagation), which was in the read direction for the axial MR images acquired in this study. The triggers for sending the ultrasonic pulses to generate the shear wave were also programmed into the MR imaging sequence. The propagation of the shear wave was imaged by acquiring a series of nine displacement (phase shift) images. Tracking the shear wave was implemented by changing t_d by increments of 0.45 ms between acquisitions. The acquisition time for each image of the propagating shear wave was 4 min and this resulted in a total of 36 min to record 9 time points as the shear wave propagated. This time can be greatly reduced by decreasing the number of views of the wave or by changing various imaging parameters in future studies. The detailed MRI acquisition parameters are listed in table 2. The residual phase map was obtained via the subtraction of a pair of phase maps acquired with inverse MEG polarity as a means to increase the SNR as well as to eliminate bulk motion and background variations (Palmeri and Nightingale 2011). The phase map was then converted to a displacement map based on the phase difference, gradient strength, encoding time and gyromagnetic ratio, as in equation (2) in Liu *et al* (2015).

The annular ultrasound array was mounted on a motorized positioning stage located within the MRI and oriented such that the beam is transmitted upward into the bore (figure 1(b)). For convenience, we invert this geometry in all subsequent figures such that the beam axis is

oriented downward as in figure 1(c). The typical field of view for the MRI images was 56 mm^2 and for sst-MRE was 52 mm^2. The MRI provides a trigger signal for the train of ultrasound pulses such that the ultrasound timing is controlled by the MRI sequence. The focal depth of the ultrasound array was updated in real time in order to create the supersonic effect, with the depth increased by 9 mm over 0.9 ms and creating an effective supersonic propagation velocity of 10 m s^{-1} as compared to the shear wave velocities of 1–4 m s^{-1} for the materials used in these phantoms (figure 1(c)). One challenging element of sst-MRE is the real-time update of the focal depth of the ultrasound array during MR imaging. In the three-pulse configuration used in the experimental results below, successive pulses differ in focal depth by 4.5 mm (with typical focal depths of 30.5 mm, 35 mm and 39.5 mm) and each pulse has a 0.45 ms duration, 42 W acoustic power and 12.5 MPa peak negative pressure (PNP) unless otherwise noted below. With the IGT system, shifting the ultrasound focus requires 0.45 ms which limits the minimum pulse spacing. We compare wavefronts generated by 1–4 pulses in the results section. When a fourth transmission was including in the supersonic pulse train, the focal depth was 44 mm with all other parameters maintained as with the three-pulse train. Based on the resulting displacement and signal strength of the generated shear wave wavefronts, a three-pulse excitation was chosen to generate displacement maps for the shear modulus studies (figure 1(c)). A typical displacement map for the propagating shear wave is shown in figure 1(d).

2.3. Ultrasound-based transient shear wave elasticity imaging

To validate the shear modulus measurement by sst-MRE, US-SWEI was also implemented on the same phantoms. As opposed to sst-MRE, which is a new protocol proposed here, US-SWEI has been previously applied in soft tissue elasticity mapping (Bercoff *et al* 2004a, 2004c). In this study, US-SWEI was performed with a commercial Phillips ATL L7-4 128-element linear array transducer with an element spacing of 0.3 mm. The probe was connected to a Verasonics ultrasound system (Vantage 256, Verasonics, WA, USA), which was programmed to both transmit and receive signals. Shear waves were generated by transmitting three consecutive pulses with a spacing of 5 mm between the transmit foci (figure 2) through the central 64 elements of the array, and each pulse has a 4.3 MHz center frequency, 100 μs duration and 10 MPa PNP. Imaging of shear wave propagation was performed using the same array using a center frequency of 5.2 MHz, with 20 acquisitions of 50 frames in a plane wave imaging mode at a PRF of 10 kHz. Shear wave displacements were tracked using 1D normalized cross-correlation with a tracking window of 2.4 mm (8 wavelengths) (Nightingale *et al* 2001). The typical field of view for the US images was 53 mm^2 and for US-SWEI was 38 mm^2.

2.4. Shear elasticity map reconstruction

A series of 2D displacement maps was obtained at different times from both the MR-based and ultrasound-based shear wave methods. The displacement and shear modulus maps are represented in a lateral-axial (depth) imaging plane with respect to the transducer generating the displacement. The displacement data are acquired with x, t, and z representing the lateral, time and axial axes, respectively. Further, Δx, Δt, and Δz are the sampling intervals and i, k, and j are the pixel indices, respectively, of the x, t and z axes, respectively. In this study, a time-of-flight (TOF) based method relying on identifying peak displacements in

space was implemented for processing the MR-tracked data. In addition, both the TOF and a LIM were implemented for the ultrasound data. All datasets were processed using Matlab (The Mathworks Inc., Natick, MA).

2.4.1. TOF-based method for processing the MR-tracked data—The implementation of the TOF-based method together with the pre-processing of the displacement data and the post-processing of the obtained shear modulus map are described below.

Before estimating the material properties based on the TOF-based method, the experimentally-acquired displacement dataset, $d(i, k, j)$, was processed with the following operations. First, the region of interest was windowed. Each acquired slice was of dimension 80 mm × 80 mm (corresponding to 240 × 240 pixels with in-plane spatial resolution of 0.333 mm); however, regions of excitation and reduced amplitude were excluded and the field of view was therefore narrowed. Elasticity was estimated in a region of 35 mm in the lateral dimension and 15 mm in the axial dimension corresponding to a 105 × 9 × 45 voxel matrix (lateral dimension x time x axial dimension). A spatial smoothing filter (Savitzky–Golay) was then applied in every slice along the lateral dimension (i.e. the direction of shear wave propagation) using a built-in Matlab function with a polynomial order of 2 and a window size of 7 pixels. Third, interpolation was performed in the time domain. The displacement-time signals of the selected dataset corresponding to specific positions of the imaging plane were interpolated by a factor of 3 yielding a 105 × 25 × 45 voxel axial displacement matrix. A directional filter was implemented as in Deffieux *et al* (2011) in order to reject reflections from the far boundary of the inclusion. Given that we are acquiring data for ~5 ms and are tracking the peak of the shear wave in the spatial domain, the impact of the directional filter on the resulting shear modulus estimates is small (<5%) in this analysis. Still, the filter is applied to improve the quality of the images presented within this paper.

To implement the TOF-based method, we first found the location of the peak displacement in the lateral dimension (figure 3(a)). We found that a customer-designed Matlab function ‘findpeaksx’ (O’Haver) was sufficient for the MRI data. The algorithm smoothed the first derivative of the signal by a window (5 pixels), detected downward zero-crossings, and then estimated the position, height and width of each peak by least-squares curve-fitting of the original unsmoothed signal in the vicinity of the zero-crossing. For the selected measurements, the ultrasound beam center corresponded to a lateral distance of 16 mm from the center of the MR coordinate system (figure 3(a)), and the generated shear wave propagated away from the excitation location as a function of time. Received data were divided into two subsets according to the direction of shear wave propagation and processed separately before the final combination into a single elasticity map. For each data subset, the locations of the peak displacement of the displacement-space signals obtained at different times were identified along the lateral axis. Figure 3(a) shows examples of the peak displacement identified from each time k with axial position indexed by j and located at distance z from the origin. We define $x_{\max}(k, j)$ as the matrix containing the corresponding position in mm of each peak and $i_{\max}(k, j)$ as the matrix containing the index corresponding to the peak locations, where

$$\forall(k,j):i_{\max}(k,j) \triangleq \text{index } i \text{ corresponding to } [\max_i d(i,k,j)], \quad (1)$$

$$x_{\max}(k,j)=i_{\max}(k,j)*(\Delta_x)-x_{\text{center}}, \quad (2)$$

and x_{center} is the center of the ultrasound excitation along the lateral dimension. The local shear wave speed, a matrix $c(i, j)$ of dimension 105 × 45, was then initialized as a null matrix and populated with values for all pixels in the imaging plane at which a peak displacement was identified in the step above, using the following equation:

$$\forall(k,j):c([i=i_{\max}(k,j)],j)=\frac{x_{\max}(k,j)-x_{\max}(k-3,j)}{3\Delta_t}, \quad (3)$$

in which Δ_t is the interpolated sampling interval in the time domain. After detecting the peak displacement along each axial line for each interpolated slice, we find a set of displacement peak locations $x_{\max}(k, j)$ of dimension 25 × 45 and values for the shear wave speed populating the $c(i, j)$ matrix of dimension 105 × 45. Third, the local shear modulus, $\mu(i, j)$, was calculated for the peak displacement positions according to the following relationship:

$$\mu(i,j)=\rho c^2(i,j), \quad (4)$$

in which the mass density of the medium material (ρ) is assumed as 1000 kg m^{-3}, a reasonable estimate for phantom materials mimicking soft tissues.

The following post-processing operations were successively applied to the shear modulus map. In each case at the edges of the imaging plane where a full 7 × 7 kernel cannot be fully applied, zero padding was added. First, a 7 × 7 median filter was applied across all nonzero values to reduce shot noise (figure 3(b)). Second, empty pixels were filled by implementing a robust gap filling algorithm (executed by a customer-designed Matlab function ‘inpaintn’ (Garcia 2017)) based on the discrete cosine transform (Garcia 2010, Wang *et al* 2012), and applying a mask defined by the region of nonzero signal (region of shear wave propagation) as shown in figure 3(c). A 7 × 7 equally-weighted averaging filter was then applied to smooth the shear elasticity map (figure 3(d)). Finally, 2D interpolation was performed to upsample the shear modulus map by a factor of 4, yielding pixels of ~83 μm by ~83 μm (figure 3(e)). Square regions of interest, with an area spanning the inclusion, were applied to estimate the shear modulus of the inclusion and the background materials of the tested phantoms.

2.4.2. Processing of ultrasound-tracked data—In processing the ultrasound-tracked data, two methods have been conventionally applied: the LIM (Bercoff *et al* 2004a, 2004b, 2004c) and the TOF method (McLaughlin and Renzi 2006a, 2006b, Palmeri *et al* 2008). In

this work, we implemented both methods in processing the ultrasound data and similar results were observed. We introduce LIM in this section and provide the results obtained using LIM in the comparison with sst-MRE results and a subset of the TOF method data. Simplifications of the linearized wave equation include: (1) the viscosity of the medium does not significantly affect the shear wave speed and therefore can be neglected, (2) the medium is purely elastic, infinite, isotropic, and locally homogenous and (3) the relationship of bulk modulus (λ) and shear modulus (μ) is $\lambda \gg \mu$. Theoretically, shear wave propagation in a homogeneous medium can be expressed as:

$$\rho \frac{\partial^2 d}{\partial t^2} = \mu \Delta d \quad (5)$$

in which ρ is the mass density of the medium, d is the displacement vector, and μ is the shear elastic modulus. As above, the external excitation was applied only in the axial (z) direction, and therefore only the axial displacement is experimentally obtained, denoted again here by d. Since imaging was performed in the lateral-axial (x–z) plane, only two of the second order derivatives in the Laplacian term can be calculated in the equation above. If the shear wave generated in the medium does not significantly diffract in the elevation direction (i.e. the y-axis), the out of plane component can be ignored. Considering that the axial displacement is a function of time t and space (x and z), the motion of the generated shear wave can be expressed as:

$$\rho \frac{\partial^2 d(x,\, t,\, z)}{\partial t^2} \approx \mu \left(\frac{\partial^2 d(x,\, t,\, z)}{\partial x^2} + \frac{\partial^2 d(x,\, t,\, z)}{\partial z^2} \right). \quad (6)$$

In the Fourier domain the local shear modulus defined above can be expressed as a function of the Fourier transform (FT) of the Laplacian and of the second derivatives of the displacement:

$$\mu(x,z) \approx \frac{\rho}{N} \sum_{\omega} \frac{\mathrm{FT}\left\{ \frac{\partial^2 d(x,t,z)}{\partial t^2} \right\}}{\mathrm{FT}\left\{ \frac{\partial^2 d(x,t,z)}{\partial x^2} + \frac{\partial^2 d(x,t,z)}{\partial z^2} \right\}}, \quad (7)$$

in which ω corresponds to the bandwidth of the excited shear wave and N is the number of frequency values used. In discrete form, the local shear modulus can be expressed as:

$$\mu(i,j) \approx \frac{\rho}{N} \sum_{\omega} \frac{\mathrm{FT}\left\{ \frac{d(i,k+1,j) - 2d(i,k,j) + d(i,k-1,j)}{\Delta_t^2} \right\}}{\mathrm{FT}\left\{ \frac{d(i+1,k,j) - 2d(i,j,k) + d(i-1,k,j)}{\Delta_x^2} + \frac{d(i,k,j+1) - 2d(i,k,j) + d(i,k,j-1)}{\Delta_z^2} \right\}}. \quad (8)$$

Thus, the local shear modulus can be obtained for each position in the imaging plane. Before implementing the LIM, the data corresponding to a region with the same size as in sst-MRE

(35 mm × 15 mm in the lateral-axial plane) were first selected and then smoothed using a Savitzky-Golay filter (a polynomial order of 2 and a window size of 7 pixels) along the wave propagation direction. After the implementation of this method, a 7 × 7 median filter (a standard function in Matlab) was first applied to the obtained shear modulus map; a 7 × 7 2D mean filter, which replaces the center element of the kernel with the equally-weight mean was then applied. Finally, the data were interpolated by a factor of 4 as in the MRI methods.

2.5. Mechanical testing of phantom materials

To further verify the reliability of sst-MRE and US-SWEI in elastographic measurement, the shear moduli of the phantom materials investigated in this work were also determined through mechanical testing. For the first three tissue-mimicking phantoms (table 1), 6 cylindrical specimens with a diameter of 26 mm and a height of ~17.5 mm (the exact height was measured during the mechanical testing) were prepared and tested in a uniaxial compressive testing performed on a universal testing system (Instron 3345, Norwood, MA, USA). Based on the Young's modulus extracted from the compressive testing, the shear modulus can be obtained according to the following relationship:

$$\mu = \frac{E}{2(1+\nu)} \cong \frac{E}{3}, \quad (9)$$

which is based on the assumption that the phantom materials are approximately incompressible and the Poisson's ratio (ν) is close to 0.5.

The procedure for the quasi-static process of the uniaxial compressive testing is summarized as follows. First, the distance between the two flat compressors of the testing system was set to 18 mm. Since this distance was larger than the actual specimen height, a dead region (with zero loading) appears in the measured load-displacement curve, which allowed for the accurate measurement of the height of each specimen. Then, the specimen was placed in the center of the flat pressor and compressed at a speed of 2 mm s^{-1} (a strain rate of ~12% s^{-1}). To estimate the Young's modulus for each sample, the recorded load-displacement data were first converted to stress–strain data and strain on the order of 4% was used for Young's modulus estimation. Linear regression was then performed on the selected portion of the stress–strain curve for each specimen and the mean values and the standard deviation a of 6 tested specimens were obtained for each phantom material.

2.6. 3D reconstruction of tumor inclusion

To fully characterize a tumor inclusion embedded in the phantom, sst-MRE was performed in five equally spaced parallel planes resulting in five shear elasticity maps. A threshold value of 13 kPa, which is larger than the shear modulus of the background (phantom) material and similar to the shear modulus measured from the inclusion (tumor), was set to identify the shape of the tumor inclusion in the extracted elasticity maps. By combining the elasticity maps from various slices, a 3D reconstruction of the properties of the embedded tumor can be obtained.

3. Results

3.1. Visualization of transient shear wave propagation using sst-MRE and US-SWEI

We began by comparing the shear wave images generated by sst-MRE as a function of the number of excitation pulses. We varied the number of transmitted pulses from 1 to 4 (the maximum allowable by the MRgFUS system in a small phantom) and compared the displacements at a delay of 1.8 ms with a 10 MPa PNP (figure 4(a)). With an increasing number of transmission pulses the resulting shear wave approaches a linear wavefront (figure 4(a)) and increased in displacement amplitude (figure 4(b)). The peak displacements using three and four excitation pulses were larger than the peak displacements with one and two foci. The peak displacements resulting from one or two excitation pulses cannot be clearly visualized at longer distances (e.g. 10 mm away from the excitations). As shown in figure 4(a)(iv) the four-pulse excitation demonstrated the highest displacement amplitude and the longest planar wavefront but required the longest time to form the planar wave. A larger echo time was therefore needed to cover a similar region with the same delay time, which reduces the SNR for this spin echo sequence. As a result of this finding, we chose to transmit three excitation pulses (figure 4(a)(iii)) for the remaining studies.

To further demonstrate the improvement in the visualization of transient shear wave propagation, the sst-MRE sequence was evaluated with varied delay time (figure 5(a)), demonstrating that the shear wave travels farther with increasing time. The propagating shear wave was readily visualized in phantom 1 with delay times from 0.45 to 4.05 ms in steps of 0.45 ms, which resulted in planar shear wave travel distances of 3 to 26 mm. The total acquisition time for each displacement map was 4 min, which resulted in a total of 36 min for all maps at 9 time delays. Shear wave propagation was also observed in the same phantom using US-SWEI with the setup shown in figure 2. A set of nine images from time points 0.4–3.6 ms was selected (figure 5(b)) to compare with MR results at similar time points.

3.2. Validation of quantitative shear modulus measurement

Next, shear modulus maps were created based on the sst-MRE and US-SWEI techniques for three phantoms (phantoms 1–3 in table 1) composed of gelatin and agar with decreasing stiffness. The shear modulus was estimated outside of the region of excitation (center of the image) and shear modulus estimates are provided in the colored parametric images based on MR (figure 6(a)) and US (figure 6(b)) methods. For phantom 1, the shear modulus was estimated as 27.3 ± 2.3 kPa (n = 3) with sst-MRE (using the TOF method based on equation (4) and associated processing). Similarly, the shear modulus estimate was 28.2 ± 2.3 kPa (n = 3) with US-SWEI (using the LIM method as described in equation (8)) and was 32.3 ± 1.8 kPa (n = 6) (figure 5(c)) based on mechanical testing. Thus, the results differed by <15% of the MT value and were not significantly different. In order to cover a wider range of material properties, we estimated the shear moduli of two additional phantoms (phantom 2 and 3 in table 1), and summarized the results in table 3. On average, the results obtained by imaging were similar to those obtained by MT and were without a systematic bias.

3.3. Shear elasticity assessment of gelatin phantom with an agar inclusion

The sst-MRE protocol was then tested on an 8% wt/v gelatin phantom with a 1% wt/v agar inclusion. 2% wt/v fiber powder was added in both gelatin and agar as scattering media for ultrasound imaging and the shear wave propagation was visualized at 9 time points from 0.45 to 4.05 ms (figure 7(a)). From parametric images (figure 7(b)) of shear modulus estimated from the shear wave images, the agar inclusion can be clearly distinguished from the gelatin background. The average shear modulus was 17.2 ± 3.2 kPa ($n = 3$) in the agar inclusion and 8.6 ± 0.1 kPa ($n = 3$) in the gelatin (figure 7(c)).

Imaging the same gelatin phantom with the US-SWEI method provided the opportunity for comparison. The propagating wave was visualized, a set of 9 images was selected (figure 8(a)) and the shear modulus estimated (figure 8(b)). The estimated shear modulus was 13.3 ± 0.4 kPa in the agar inclusion ($n = 3$) and 8.3 ± 0.3 kPa in the gelatin ($n = 3$) (figure 8(c)) with the sample rotated between data acquisitions. Shear moduli estimated in the gelatin background were consistent between slices and the successive estimates in the inclusion ranged from 12.9 to 13.7 kPa.

As noted previously, the US-SWEI data were processed with both the LIM and TOF method and the results were similar. For example, the estimated shear moduli obtained with the TOF method in the gelatin and inclusion in figure 8 are 8.4 kPa and 13.5 kPa, respectively, which vary from those obtained with LIM method by 0.1 kPa and 0.2 kPa, respectively. In addition, for homogenous phantoms such as phantom 2 and 3 in table 1, the shear modulus obtained with TOF methods are 12.6 kPa and 7.6 kPa, respectively, which are similar to those obtained with the LIM (12.5 kPa and 7.9 kPa, respectively) in figure 8.

3.4. sst-MRE of a gelatin phantom with an agar inclusion

To investigate the accuracy of MR-based shear modulus estimation as a function of position within the inclusion, five MR datasets were acquired with 1 mm spacing between acquisitions, as shown in figure 9(a). For each slice, a set of 9 displacement maps were generated (figure 9(b)), with t_d ranging from 0.45 to 4.05 ms. The displacement maps were converted into a shear elasticity map using the TOF-based method and finally, five elasticity maps (figure 9(c)) were generated corresponding to each of the slices, with the magnitude images shown in the first column and the corresponding elasticity maps shown in the second column. The estimated shear moduli are summarized in figure 9(d) with an average value of 4.9 ± 0.2 kPa in the 8% gelatin and 22.5 ± 4.7 kPa in the 2% agar inclusion. The shear modulus among the 5 slices was similar in the 8% gelatin with a difference of less than 1%.

3.5. sst-MRE of gelatin phantom with a tumor inclusion and the 3D tumor reconstruction

3D mapping of a tumor was then accomplished by sst-MRE using a roughly spherical neu deletion (NDL) tumor within an 8% gelatin phantom (phantom 6 in table 1). Similar to the study described in section 3.4, four images were acquired spanning the tumor diameter with 1 mm spacing. Figure 10(a) compares five MR images of the tumor inclusion (the first row) and their corresponding shear elasticity maps (the next five rows). The estimated shear modulus was 4.9 ± 0.1 kPa in 8% gelatin and 17.9 ± 4.4 kPa in the NDL tumor (figure 10(b)). With a threshold of 10 kPa, the tumor was approximately reconstructed in 3D (figure

10(c)) based on the elasticity maps. The volume of the reconstructed tumor was 121 mm^3 based on the shear modulus map and 108 mm^3 based on the MRI images.

4. Discussion

4.1. Shear wave generation in sst-MRE

For the first time, supersonic techniques were incorporated into MR-based shear wave imaging and quantitative elastography. As opposed to conventional MRE, in which a harmonic shear wave is excited in the medium by an external vibrator, sst-MRE uses a transient wave generated by ARF. The supersonic technique creates quasi-planar shear waves by moving the focal depth of the shear wave excitation at a supersonic speed (Bercoff *et al* 2004c). This is accomplished by rapidly transmitting successive excitation pulses for which the focal depth increases. The resulting quasi-planar shear wave is higher in amplitude than that generated from a single excitation, as is used in conventional t-MRE (Souchon *et al* 2008, Liu *et al* 2015), and the properties of the media are simply visualized and quantified due to the planar geometry. The sst-MRE protocol here utilizes the same MRgFUS system to ablate tissue, monitor temperature and to generate the quasi-planar shear wave for the quantification of tissue elasticity and the extent of ablation. Therefore, without moving the patient or transducer, the ablated region can be assessed. This is important as positioning the patient and transducer for such studies requires a long and involved protocol. MRgFUS systems are growing in their clinical impact and indications and have major advantages for focal ablative procedures in that an entire 3D volume is imaged for guidance and evaluation of tissues in the path of the ultrasound beam and temperature estimation algorithms are robust and can monitor ablative temper atures. Thus, the development of methods to monitor changes in elasticity are of particular value. While US-SWEI systems can assess tissue stiffness changes following ablation, these systems cannot currently provide a full 3D view of the beam propagation path and the ability to accurately assess ablative temperatures has not been established. Further, displacement images acquired by MRI are not subject to speckle and therefore have the potential to improve the signal-to-noise ratio. This is important for mapping small changes in material properties and may be useful in the assessment of complex structures. When imaging deep tissues in large animal or human patients, higher spatial resolution may be possible with the sst-MRE method since US-SWEI will require a lower frequency to image these targets (as compared to superficial targets) while MRI resolution is independent of tissue depth.

An additional advantage of this supersonic regimen is that it can be applied to interrogate the same region of interest from different angles of view by changing the orientation of the planar wavefront of the generated shear wave through varying the locations and timing of the excitations. In a multiple-pulse excitation, by spacing the excitation focal depths by 4.5 mm and changing the time of transmission (which is the pulse duration at each location) by 0.45 ms, the effective speed of the moving source is 10 m s^{-1}. If the shear wave propagation speed in the medium is 5.8 m s^{-1}, the wavefront of the resulting planar shear wave is tilted ~30° from longitudinal wave axis. If a smaller steering angle is desired in the measurement, the following two methods can be considered. One method to decrease the steering angle is to increase the source speed by spacing the sources further apart along the excitation axis

while keeping the pulse length the same. The drawback of this method is that the strength of the shear wave will be reduced. The other method is to reduce the inter-pulse transmission time (and therefore the pulse length). However, the current minimum pulse length in the constructive multi-pulse mode is ~0.45 ms due to hardware limitations and therefore only a limited range of angles can be achieved.

Using the new sst-MRE sequence, we observed the shear wave travelling over distances between 2 and 30 mm. In our previous work using an MR-ARFI sequence, we could not visualize propagation distances smaller than 10 mm due to the time required by the ultrasound excitation and MEGs (in total more than 13.5 ms) (Liu *et al* 2015). Here, our ability to visualize the shear wave within millimeters from the location of the excitation and the quasiplanar nature of the propagating wave improve our ability to apply the technique in phantom mat erials, small target organs, small lesions or regions of inhomogeneity.

We demonstrated that this MR-based technique can provide 3D visualization of the tissue elasticity. To demonstrate this capability of MR-based imaging in sst-MRE, shear elasticity maps of a series of slices were obtained for both the gelatin phantom with agar inclusion (figure 9) and the gelatin phantom with tumor inclusion (figure 10). Based on these elasticity maps, a 3D reconstruction of the inclusion can be created given a predefined elasticity boundary. As an example, the 3D shape of the tumor inclusion based on the shear elasticity maps was reconstructed and shown in figure 10.

4.2. Imaging time and gradient strength required for sst-MRE

The total acquisition time required for the current MR implementation of the sst-MRE technique is substantial; however, this can be reduced. For a 240 × 240 matrix, 36 min were required to acquire 9 sst-MRE images; however, all 9 delays are not necessary to generate the shear elasticity map. For example, using 5 delay times, the current imaging protocol can generate a shear map in ~20 min. The acquisition parameters can also be modified to reduce the time required, including reducing the number of images, repetition time and matrix size to reduce the imaging time. Incorporating a surface or phased array coil is another option to reduce imaging time without sacrificing SNR. Other MRE techniques could also be considered. For instance, a gradient echo phase contrast MRI sequence including an additional MEG could be applied (Souchon *et al* 2008). Echo planar imaging (EPI)-based sequence is another choice to shorten imaging time; however, such techniques are challenging at 7 T due to shim effects (Kaye *et al* 2011). Although not applied here, we have also investigated the use of a spiral readout to reduce the acquisition speed from 2 min for a single slice (MSME protocol) to 10 s for 9 slices (spiral readout), which shortens the total acquisition time eight fold while also providing 3D information on the shear wave propagation. There is a cost in signal-to-noise ratio and potential artifacts and therefore we chose to present data here with a standard imaging sequence and optimize fast imaging in future work. Based on scans with fewer delay times and spiral readouts, a practical clinical approach is feasible with a scan time of 2–4 min. Current clinical MRgFUS studies often require ~5 h with as little as half of the MR room time dedicated to treatment on average (Kim *et al* 2012). The inclusion of an sst-MRE protocol would be feasible during non-treatment times that do not require active MR scanning (e.g. treatment planning, registration

with pre-acquired computed tomography, or cooling). We recognize that the minutes required for sst-MRE is greater than the 10 ms required for acquisition of 50 frames using US-SWEI. However, the added time for the sst-MRE protocol, which is performed by the same system as the ablation, is insignificant compared to removing the patient from the MRgFUS ablation setup and performing the US-SWEI procedure on a separate system.

The imaging gradients available on our 7 T scanner are more sensitive than those available on lower field scanners. However, the sensitivity to displacement is linearly dependent upon the total gradient area (integral of the gradient waveform) of the MEGs. Thus, equivalent motion sensitivity can be achieved with a weaker gradient by increasing the gradient duration. Given that other shear wave and ARFI techniques have been realized on 1.5 and 3 T MRI systems, the potential for this technique to be realized is high.

4.3. Image processing methods for generating a shear modulus map

The conventional inversion methods for reconstructing a shear elasticity map from a series of displacement maps obtained either by MR or ultrasound imaging techniques, are based on solving the simplified equation of wave propagation under the assumption of local homogeneity (LIM) or identifying the TOF of the generated shear wave (TOF-based method). In this work, we implemented both the LIM and the TOF method for processing the ultrasound tracked displacement data and found that the results were similar. For processing the displacement maps obtained using the sst-MRE technique, neither the conventional LIM nor the conventional TOF-based method can produce accurate elasticity images due to the limited number of measurements in the time domain. Therefore, a TOF-based method was developed by tracking the shear wave peaks in the spatial domain (rather than in the time domain as implemented in the conventional TOF-based method). The advantage of this method is it can effectively process a dataset with a smaller number of displacement images and therefore facilitates the application of the MR-guided transient shear wave imaging proposed in this work.

4.4. Validation of sst-MRE in quantitative shear modulus measurements and the application in lesion detection

An important goal of this work is to validate the proposed sst-MRE technique in quantitatively accessing the elasticity of tissue-mimicking phantoms and soft tissues. For this purpose, US-SWEI was implemented on the same three phantoms (phantoms 1–3 in table 1) that were tested using sst-MRE; compressive mechanical testing was also performed on the specimens made of the same materials as those of the three types of the phantoms. Obtaining elasticity estimates using mechanical testing is challenging for tissue and tissue-mimicking phantom materials; measurements within a reasonable range have been reported under the small strain assumption (Madsen *et al* 2003, Madsen *et al* 2005, Madsen *et al* 2006). Cross-validation between mechanical testing and ultrasound-based transient elastographic techniques has previously been reported for shear elasticity measurements (Oudry *et al* 2009). The comparison of the results obtained here using these three techniques shown in figure 6 and table 3 suggests that there is no significant difference among the shear elasticity measurements obtained using different methods and therefore verifies the capability and reliability of the sst-MRE technique in quantitative elasticity assessment.

Moreover, the consistency of sst-MRE in shear elasticity measurements can be observed by comparing the shear modulus measurements between phantom 3 (table 3) and phantom 4 (figure 7) and between phantom 5 (figure 9) and phantom 6 (figure 10), which share the same background materials.

We demonstrated the capability of the sst-MRE technique in detecting inclusions within tissue-mimicking phantoms. The measurements on phantom 4 (figure 7), phantom 5 (figure 9) and phantom 6 (figure 10) clearly show the elasticity difference between the inclusions (agar and tumor) and the background materials. As to the accuracy in the inclusion elasticity measurement, the US-SWEI measurement in figure 8 shows comparable results to the sst-MRE measurement in figure 7.

5. Conclusions

In this study, we have demonstrated a supersonic transient MRE protocol using the combination of an MR shear imaging sequence and multi-pulse transmission. The new technique was applied to improve the visualization of shear wave propagation and quantify tissue mechanical properties. Quantitative mapping of shear modulus is feasible *in vitro* and the estimated shear moduli showed no significant differences between sst-MRE and US-SWEI and MT. Also, a 3D tumor map was reconstructed based on the 2D elasticity maps. The new sst-MRE protocol described here has potential application for monitoring tissue stiffness during ablative treatments. Ongoing work is aimed at the detection of ablation foci.

Acknowledgments

This work was supported by NIHR01CA112356, NIHR01CA134659, NIHR01CA210553 and NIH R01CA199658.

References

Aguilo MA, Aquino W, Brigham JC, Fatemi M. An inverse problem approach for elasticity imaging through vibroacoustics. IEEE Trans Med Imaging. 2010; 29:1012–21. [PubMed: 20335092]

Bamber J, et al. EFSUMB guidelines and recommendations on the clinical use of ultrasound elastography. Part 1: basic principles and technology. Ultraschall Med. 2013; 34:169–84. [PubMed: 23558397]

Barton MB, Harris R, Fletcher SW. Does this patient have breast cancer? The screening clinical breast examination: should it be done? How? J Am Med Assoc. 1999; 282:1270–80.

Bavu E, et al. Noninvasive *in vivo* liver fibrosis evaluation using supersonic shear imaging: a clinical study on 113 hepatitis C virus patients. Ultrasound Med Biol. 2011; 37:1361–73. [PubMed: 21775051]

Bercoff J, Pernot M, Tanter M, Fink M. Monitoring thermally-induced lesions with supersonic shear imaging. Ultrason Imaging. 2004a; 26:71–84. [PubMed: 15344412]

Bercoff J, Tanter M, Fink M. Local inversion of transient shear wave propagation for elasticity and viscosity mapping in soft tissues: theoretical and experimental analysis. IEEE Ultrasonics Symp. 2004b; 1–3:2149–52.

Bercoff J, Tanter M, Fink M. Supersonic shear imaging: a new technique for soft tissue elasticity mapping. IEEE Trans Ultrason Ferroelectr Freq Control. 2004c; 51:396–409. [PubMed: 15139541]

Brock M, Eggert T, Loppenberg B, Braun K, Roghmann F, Palisaar RJ, Noldus J, von Bodman C. Value of real-time elastography to guide the systematic prostate biopsy in men with normal digital rectal exam. Aktuelle Urol. 2013; 44:40–4. [PubMed: 23325671]

Bude RO, Adler RS. An easily made, low-cost, tissue-like ultrasound phantom material. J Clin Ultrasound. 1995; 23:271–3. [PubMed: 7797668]

Cespedes I, Ophir J, Ponnekanti H, Maklad N. Elastography: elasticity imaging using ultrasound with application to muscle and breast *in vivo*. Ultrason Imaging. 1993; 15:73–88. [PubMed: 8346612]

Chen S, et al. Assessment of liver viscoelasticity by using shear waves induced by ultrasound radiation force. Radiology. 2013; 266:964–70. [PubMed: 23220900]

Cho SH, Lee JY, Han JK, Choi BI. Acoustic radiation force impulse elastography for the evaluation of focal solid hepatic lesions: preliminary findings. Ultrasound Med Biol. 2010; 36:202–8. [PubMed: 20018432]

Choi JJ, Kang BJ, Kim SH, Lee JH, Jeong SH, Yim HW, Song BJ, Jung SS. Role of sonographic elastography in the differential diagnosis of axillary lymph nodes in breast cancer. J Ultrasound Med. 2011; 30:429–36. [PubMed: 21460142]

Cosgrove D, et al. EFSUMB guidelines and recommendations on the clinical use of ultrasound elastography. Part 2: clinical applications. Ultraschall Med. 2013; 34:238–53. [PubMed: 23605169]

Deffieux T, Gennisson JL, Bercoff J, Tanter M. On the effects of reflected waves in transient shear wave elastography. IEEE Trans Ultrason Ferroelectr Freq Control. 2011; 58:2032–5. [PubMed: 21989866]

Duck, FA. Physical Properties of Tissues. London: Academic; 1990.

Fite BZ, Liu Y, Kruse DE, Caskey CF, Walton JH, Lai CY, Mahakian LM, Larrat B, Dumont E, Ferrara KW. Magnetic resonance thermometry at 7T for real-time monitoring and correction of ultrasound induced mild hyperthermia. PLoS One. 2012; 7:e35509. [PubMed: 22536396]

Friedman SL. Evolving challenges in hepatic fibrosis. Nat Rev Gastroenterol Hepatol. 2010; 7:425–36. [PubMed: 20585339]

Friedrich-Rust M, Ong MF, Martens S, Sarrazin C, Bojunga J, Zeuzem S, Herrmann E. Performance of transient elastography for the staging of liver fibrosis: a meta-analysis. Gastroenterology. 2008; 134:960–74. [PubMed: 18395077]

Garcia, D. 2017. www.mathworks.com/matlabcentral/fileexchange/27994-inpaint-over-missing-data-in-1-d-2-d-3-d-n-d-arrays/content/inpaintn.m

Garcia D. Robust smoothing of gridded data in one and higher dimensions with missing values. Comput Stat Data Anal. 2010; 54:1167–78. [PubMed: 24795488]

Garra BS, Cespedes EI, Ophir J, Spratt SR, Zuurbier RA, Magnant CM, Pennanen MF. Elastography of breast lesions: initial clinical results. Radiology. 1997; 202:79–86. [PubMed: 8988195]

Giovannini M, et al. Endoscopic ultrasound elastography for evaluation of lymph nodes and pancreatic masses: a multicenter study. World J Gastroenterol. 2009; 15:1587–93. [PubMed: 19340900]

Itoh A, Ueno E, Tohno E, Kamma H, Takahashi H, Shiina T, Yamakawa M, Matsumura T. Breast disease: clinical application of US elastography for diagnosis. Radiology. 2006; 239:341–50. [PubMed: 16484352]

Janssen J, Dietrich CF, Will U, Greiner L. Endosonographic elastography in the diagnosis of mediastinal lymph nodes. Endoscopy. 2007; 39:952–7. [PubMed: 18008203]

Kallel F, Bertrand M. Tissue elasticity reconstruction using linear perturbation method. IEEE Trans Med Imaging. 1996; 15:299–313. [PubMed: 18215911]

Kaye EA, Chen J, Pauly KB. Rapid MR-ARFI method for focal spot localization during focused ultrasound therapy. Magn Reson Med. 2011; 65:738–43. [PubMed: 21337406]

Kim YS, Keserci B, Partanen A, Rhim H, Lim HK, Park MJ, Kohler MO. Volumetric MR-HIFU ablation of uterine fibroids: role of treatment cell size in the improvement of energy efficiency. Eur J Radiol. 2012; 81:3652–9. [PubMed: 21959213]

Kirk GD, et al. Assessment of liver fibrosis by transient elastography in persons with hepatitis C virus infection or HIV-hepatitis C virus coinfection. Clin Infect Dis. 2009; 48:963–72. [PubMed: 19236273]

Konofagou EE, Maleke C, Vappou J. Harmonic motion imaging (HMI) for tumor imaging and treatment monitoring. Curr Med Imaging Rev. 2012; 8:16–26. [PubMed: 25364321]

Lerner RM, Huang SR, Parker KJ. 'Sonoelasticity' images derived from ultrasound signals in mechanically vibrated tissues. Ultrasound Med Biol. 1990; 16:231–9. [PubMed: 1694603]

Liu Y, Fite BZ, Mahakian LM, Johnson SM, Larrat B, Dumont E, Ferrara KW. Concurrent visualization of acoustic radiation force displacement and shear wave propagation with 7T MRI. PLoS One. 2015; 10:e0139667. [PubMed: 26439259]

Lizzi FL, Muratore R, Deng CX, Ketterling JA, Alam SK, Mikaelian S, Kalisz A. Radiation-force technique to monitor lesions during ultrasonic therapy. Ultrasound Med Biol. 2003; 29:1593–605. [PubMed: 14654155]

Lyshchik A, Higashi T, Asato R, Tanaka S, Ito J, Hiraoka M, Insana MF, Brill AB, Saga T, Togashi K. Cervical lymph node metastases: diagnosis at sonoelastography—initial experience. Radiology. 2007; 243:258–67. [PubMed: 17293571]

Madsen EL, Frank GR, Hobson MA, Shi H, Jiang J, Varghese T, Hall TJ. Spherical lesion phantoms for testing the performance of elastography systems. Phys Med Biol. 2005; 50:5983–95. [PubMed: 16333168]

Madsen EL, Frank GR, Krouskop TA, Varghese T, Kallel F, Ophir J. Tissue-mimicking oil-in-gelatin dispersions for use in heterogeneous elastography phantoms. Ultrason Imaging. 2003; 25:17–38. [PubMed: 12747425]

Madsen EL, Hobson MA, Frank GR, Shi H, Jiang J, Hall TJ, Varghese T, Doyley MM, Weaver JB. Anthropomorphic breast phantoms for testing elastography systems. Ultrasound Med Biol. 2006; 32:857–74. [PubMed: 16785008]

McCracken PJ, Manduca A, Felmlee J, Ehman RL. Mechanical transient-based magnetic resonance elastography. Magn Reson Med. 2005; 53:628–39. [PubMed: 15723406]

McLaughlin J, Renzi D. Shear wave speed recovery in transient elastography and supersonic imaging using propagating fronts. Inverse Problems. 2006a; 22:681–706.

McLaughlin J, Renzi D. Using level set based inversion of arrival times to recover shear wave speed in transient elastography and supersonic imaging. Inverse Problems. 2006b; 22:707–25.

Muthupillai R, Lomas DJ, Rossman PJ, Greenleaf JF, Manduca A, Ehman RL. Magnetic resonance elastography by direct visualization of propagating acoustic strain waves. Science. 1995; 269:1854–7. [PubMed: 7569924]

Muthupillai R, Rossman PJ, Lomas DJ, Greenleaf JF, Riederer SJ, Ehman RL. Magnetic resonance imaging of transverse acoustic strain waves. Magn Reson Med. 1996; 36:266–74. [PubMed: 8843381]

Nightingale K, Soo MS, Nightingale R, Trahey G. Acoustic radiation force impulse imaging: *in vivo* demonstration of clinical feasibility. Ultrasound Med Biol. 2002; 28:227–35. [PubMed: 11937286]

Nightingale KR, Palmeri ML, Nightingale RW, Trahey GE. On the feasibility of remote palpation using acoustic radiation force. J Acoust Soc Am. 2001; 110:625–34. [PubMed: 11508987]

Ophir J, Cespedes I, Ponnekanti H, Yazdi Y, Li X. Elastography: a quantitative method for imaging the elasticity of biological tissues. Ultrason Imaging. 1991; 13:111–34. [PubMed: 1858217]

Oudry J, Bastard C, Miette V, Willinger R, Sandrin L. Copolymer-in-oil phantom materials for elastography. Ultrasound Med Biol. 2009; 35:1185–97. [PubMed: 19427100]

Palmeri ML, Nightingale KR. Acoustic radiation force-based elasticity imaging methods. Interface Focus. 2011; 1:553–64. [PubMed: 22419986]

Palmeri ML, Wang MH, Dahl JJ, Frinkley KD, Nightingale KR. Quantifying hepatic shear modulus *in vivo* using acoustic radiation force. Ultrasound Med Biol. 2008; 34:546–58. [PubMed: 18222031]

Plewes DB, Bishop J, Samani A, Sciarretta J. Visualization and quantification of breast cancer biomechanical properties with magnetic resonance elastography. Phys Med Biol. 2000; 45:1591–610. [PubMed: 10870713]

Salomon G, Kollerman J, Thederan I, Chun FK, Budaus L, Schlomm T, Isbarn H, Heinzer H, Huland H, Graefen M. Evaluation of prostate cancer detection with ultrasound real-time elastography: a comparison with step section pathological analysis after radical prostatectomy. Eur Urol. 2008; 54:1354–62. [PubMed: 18374470]

Sandrin L, et al. Transient elastography: a new noninvasive method for assessment of hepatic fibrosis. Ultrasound Med Biol. 2003; 29:1705–13. [PubMed: 14698338]

Sarvazyan A, Hall TJ, Urban MW, Fatemi M, Aglyamov SR, Garra BS. An overview of elastography—an emerging branch of medical imaging. Curr Med Imaging Rev. 2011; 7:255–82. [PubMed: 22308105]

Sarvazyan AP, Rudenko OV, Swanson SD, Fowlkes JB, Emelianov SY. Shear wave elasticity imaging: a new ultrasonic technology of medical diagnostics. Ultrasound Med Biol. 1998; 24:1419–35. [PubMed: 10385964]

Sarvazyan AP, Skovoroda AR, Emelianov SY, Fowlkes JB, Pipe JG, Adler RS, Buxton RB, Carson PL. Biophysical bases of elasticity imaging. Acoust Imaging. 1995; 21:223–40.

Souchon R, Salomir R, Beuf O, Milot L, Grenier D, Lyonnet D, Chapelon JY, Rouviere O. Transient MR elastography (t-MRE) using ultrasound radiation force: theory, safety, and initial experiments *in vitro*. Magn Reson Med. 2008; 60:871–81. [PubMed: 18816871]

Tanter M, Bercoff J, Athanasiou A, Deffieux T, Gennisson JL, Montaldo G, Muller M, Tardivon A, Fink M. Quantitative assessment of breast lesion viscoelasticity: initial clinical results using supersonic shear imaging. Ultrasound Med Biol. 2008; 34:1373–86. [PubMed: 18395961]

Tsutsumi M, Miyagawa T, Matsumura T, Kawazoe N, Ishikawa S, Shimokama T, Shiina T, Miyanaga N, Akaza H. The impact of real-time tissue elasticity imaging (elastography) on the detection of prostate cancer: clinicopathological analysis. Int J Clin Oncol. 2007; 12:250–5. [PubMed: 17701002]

Urban MW, Alizad A, Aquino W, Greenleaf JF, Fatemi M. A review of vibro-acoustography and its applications in medicine. Curr Med Imaging Rev. 2011; 7:350–9. [PubMed: 22423235]

Walz J, Marcy M, Pianna JT, Brunelle S, Gravis G, Salem N, Bladou F. Identification of the prostate cancer index lesion by real-time elastography: considerations for focal therapy of prostate cancer. World J Urol. 2011; 29:589–94. [PubMed: 21614469]

Wang GJ, Garcia D, Liu Y, de Jeu R, Dolman AJ. A three-dimensional gap filling method for large geophysical datasets: application to global satellite soil moisture observations. Environ Modelling Softw. 2012; 30:139–42.

Wong AW, et al. Ultrasound ablation enhances drug accumulation and survival in mammary carcinoma models. J Clin Invest. 2016; 126:99–111. [PubMed: 26595815]

Wu T, Felmlee JP, Greenleaf JF, Riederer SJ, Ehman RL. MR imaging of shear waves generated by focused ultrasound. Magn Reson Med. 2000; 43:111–5. [PubMed: 10642737]

Yeh WC, Li PC, Jeng YM, Hsu HC, Kuo PL, Li ML, Yang PM, Lee PH. Elastic modulus measurements of human liver and correlation with pathology. Ultrasound Med Biol. 2002; 28:467–74. [PubMed: 12049960]

Zhi H, Ou B, Luo BM, Feng X, Wen YL, Yang HY. Comparison of ultrasound elastography, mammography, and sonography in the diagnosis of solid breast lesions. J Ultrasound Med. 2007; 26:807–15. [PubMed: 17526612]

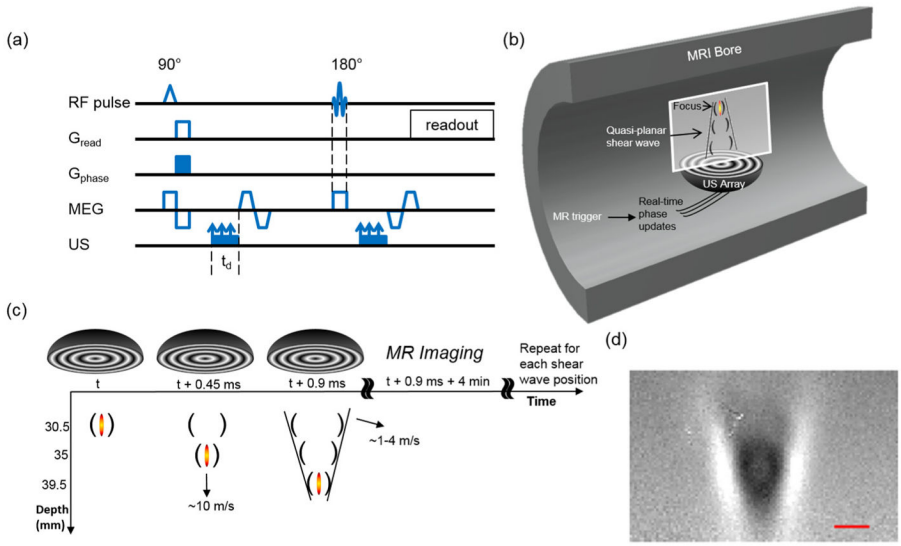

Figure 1.

Overview of the experiments. (a) sst-MRE sequence. The illustrated sequence was acquired with both positive and negative bipolar MEGs. Three successive ultrasound excitations were triggered before the MEGs. By varying the time delay t_d, a series of displacement images (TR/TE/FA = 500 ms/26.1 ms/90°) was acquired to estimate shear wave velocity. (b) Experimental diagram for sst-MRE. Annular ultrasound array was mounted within MRI to generate supersonic shear waves oriented upward vertically. Each element of the array was excited with a relative phasing that was updated in real time to achieve the various focal depths. (c) Ultrasound pulses and shear wave timing and orientation. Three pulses (3 MHz, 0.45 ms pulses with 4.5 mm spacing between transmit foci, 42 W acoustic power, 12.5 MPa PNP) were sequentially excited along the beam axis creating quasi-planar shear waves in the imaging plane. The downward propagation orientation is used throughout the paper for convenience. Diagram Reproduced from Bercoff *et al* (2004c), © 2017 IEEE. Reprinted, with permission, from IEEE. (d) Example of displacement map. The scale bar represents 5 mm.

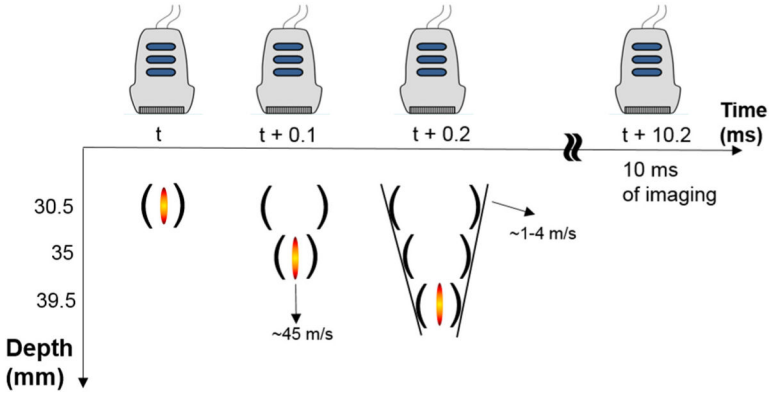

Figure 2.

Ultrasound-based transient shear wave elasticity imaging setup. Three pulses (64 elements, 4.3 MHz, 100 μs pulses with 4.5 mm spacing between transmit foci, 10 MPa PNP) were sequentially focused along the beam axis creating quasi-planar shear waves in the imaging plane. A series of displacement images was then acquired using the same array working at 5.2 MHz with 20 acquisitions of 50 frames in flash imaging mode at a PRF of 10 kHz. Diagram Reproduced from Bercoff *et al* (2004c), © 2017 IEEE. Reprinted, with permission, from IEEE.

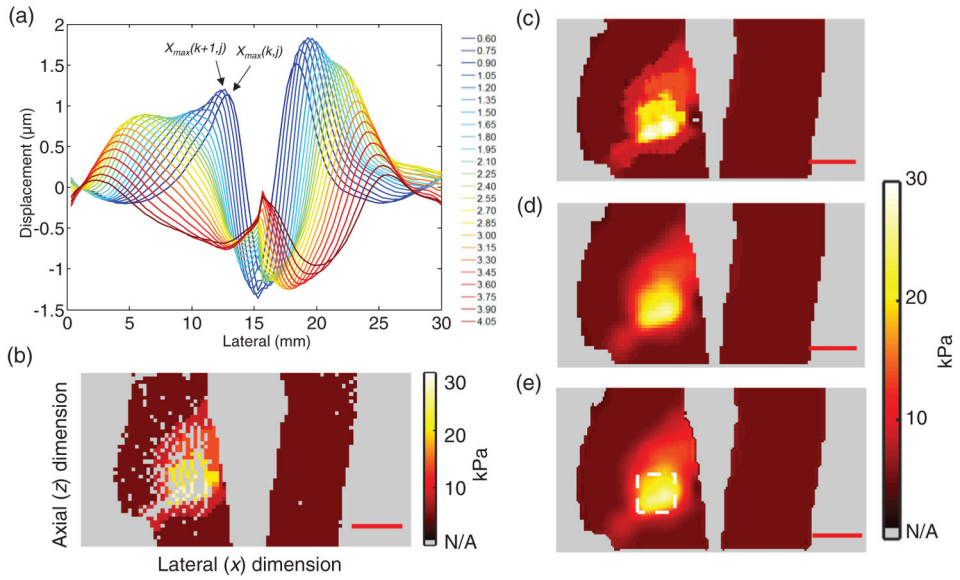

Figure 3.

Demonstration of the TOF-based shear elasticity reconstruction method for sst-MRE using a set of displacement measurements of a gelatin phantom with an agar inclusion. (a) The displacement at 24 interpolated times as the shear wave propagates laterally away from the excitation at 16 mm. The peak locations were identified and a subset is indicated here. (b) The median-filtered extracted shear modulus map. (c)–(e) Shear modulus maps after post-processing procedures: (c) interpolation to x–y grid, (d) smoothing and (e) spatial upsampling. Square indicates the region of interest for evaluating the shear moduli of the inclusion.

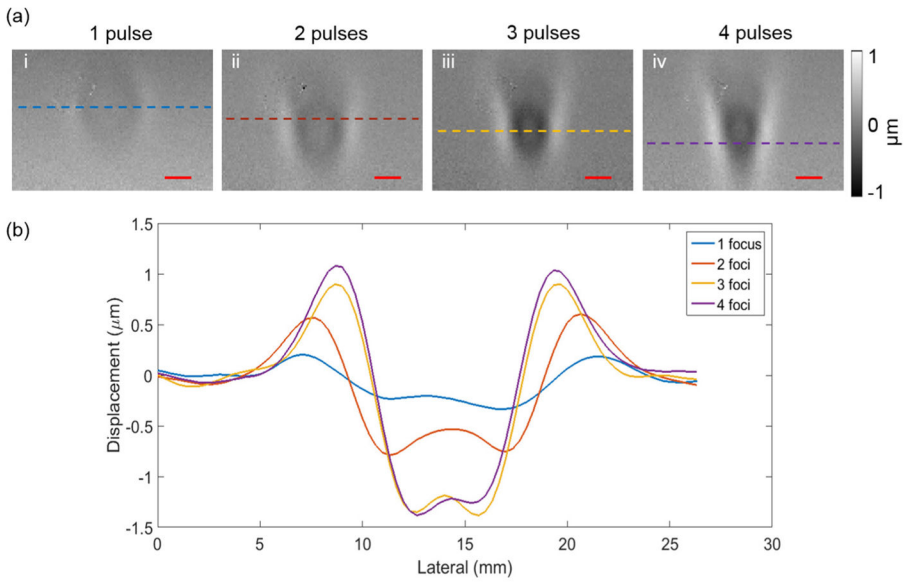

Figure 4.

Comparison of the shear waves at 1.8 ms after the start of the first excitation pulse as generated with various transmitted pulses. (a) MR displacement images of the shear waves resulting from 1, 2, 3 or 4 constructive pulses. The scale bars represent 5 mm. (b) Comparison of the lateral displacement profiles at the same axial position.

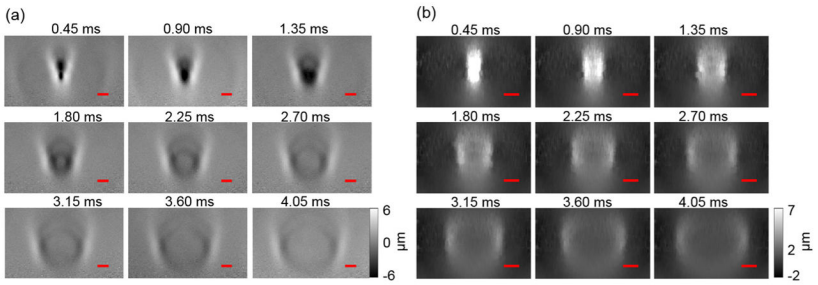

Figure 5.

Visualization of shear wave propagation in sst-MRE and US-SWEI. (a) Typical MR images of the propagating shear wave in sst-MRE. (b) A set of nine images of the propagating shear wave in US-SWEI. These images were selected at similar time delays. The scale bars represent 5 mm.

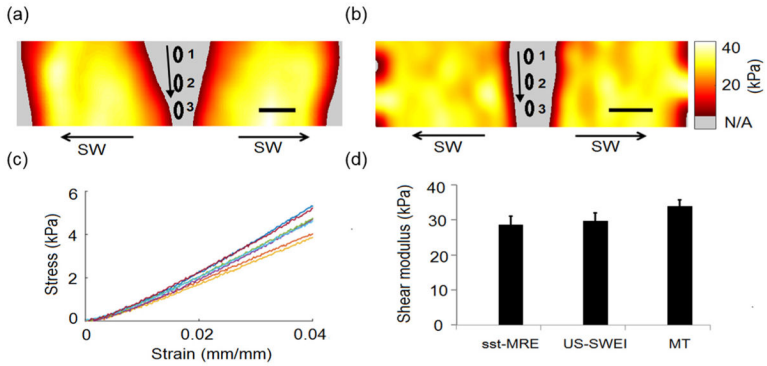

Figure 6.

Comparison of the shear modulus of phantom 1 measured by sst-MRE, US-SWEI and MT. (a) MR elasticity map using the TOF method. (b) Ultrasound elasticity map using the LIM. (c) Six mechanical testing results. (d) The estimated shear moduli (mean ± standard deviation) were 27.3 ± 2.3 (n = 3), 28.2 ± 2.3 (n = 3) and 32.3 ± 1.8 kPa (n = 6) for t-MRE, US-SWEI and MT measurements, respectively. The scale bars represent 5 mm.

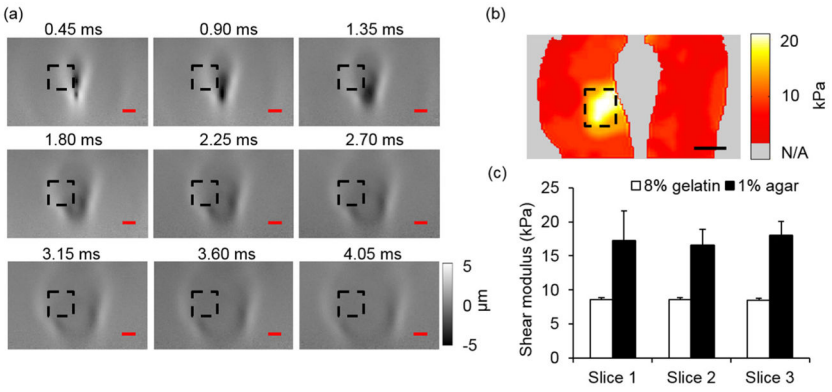

Figure 7.

Shear modulus estimation in an 8% gelatin phantom with 1% agar inclusion (phantom 4 in table 1) using sst-MRE. (a) Shear wave images from 0.45 to 4.05 ms. (b) Parametric image of the shear modulus using the TOF-based method. (c) Comparison of the estimated shear moduli in both gelatin and agar inclusions obtained from three successive slices. The scale bars represent 5 mm.

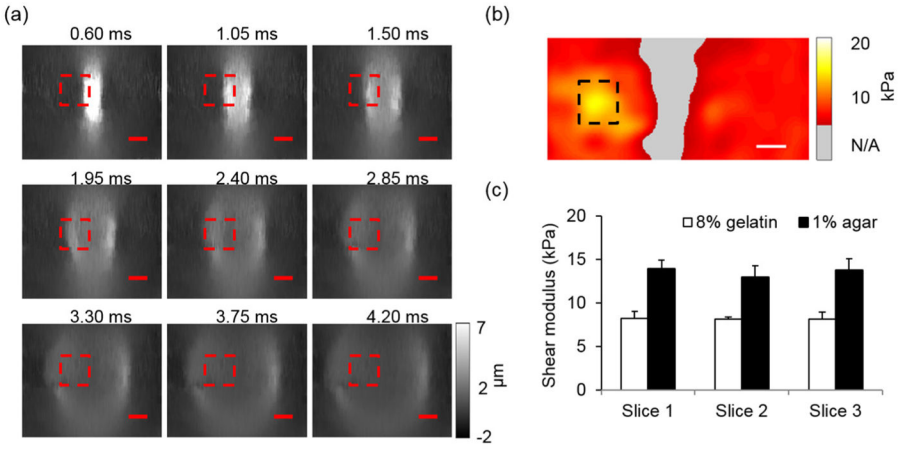

Figure 8.

Shear modulus estimation in an 8% gelatin phantom with 1% agar inclusion (phantom 4 in table 1) using US-SWEI. (a) Nine shear wave images at times ranging from 0.6 to 4.2 ms. (b) Parametric image of shear modulus using LIM. (c) Comparison of the estimated shear moduli in both gelatin and agar obtained from the measurements with the imaging plane rotated by approximately 90 degrees between repetitions. Scale bars represent 5 mm.

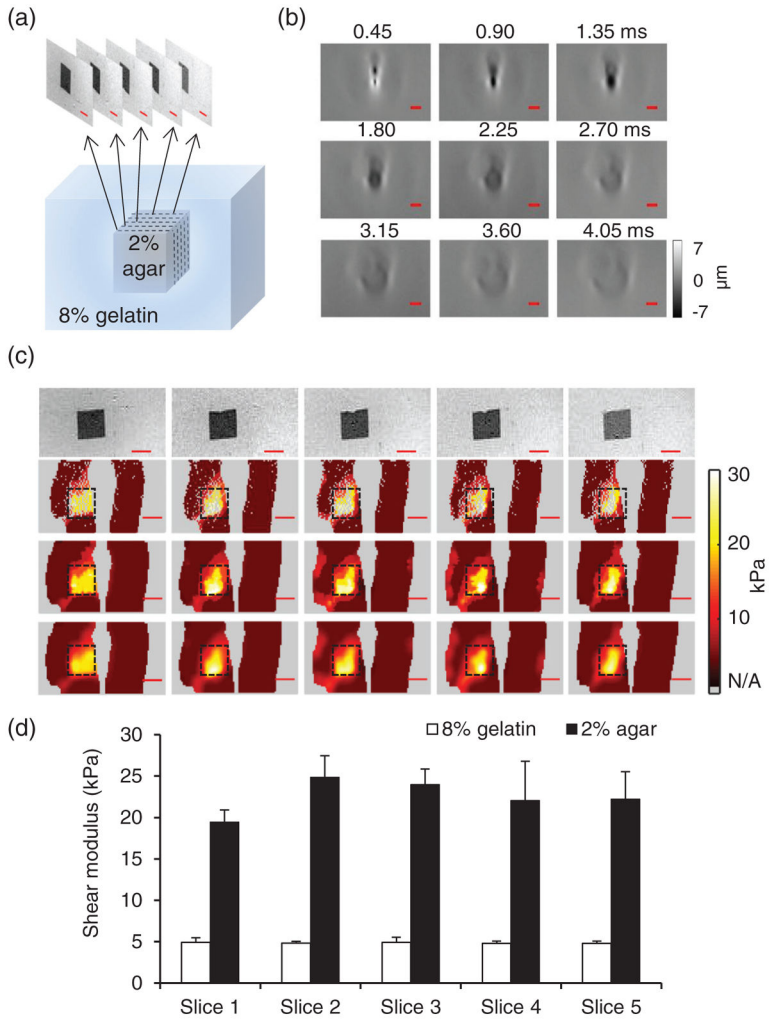

Figure 9.

Example of sst-MRE in an 8% gelatin phantom with 2% agar inclusion. (a) Imaging setup. Five magnitude images were acquired with 1 mm spacing. (b) Nine consecutive displacement maps at different time delays from 0.45 ms to 4.05 ms with a 0.45 ms spacing. (c) Five slices of MR magnitude images (the first row) and the corresponding elasticity maps (the second row to the fourth row) showing the step-by-step processing as in figure 3. (d) The summarized shear moduli in the gelatin and agar inclusion. The scale bars represent 5 mm.

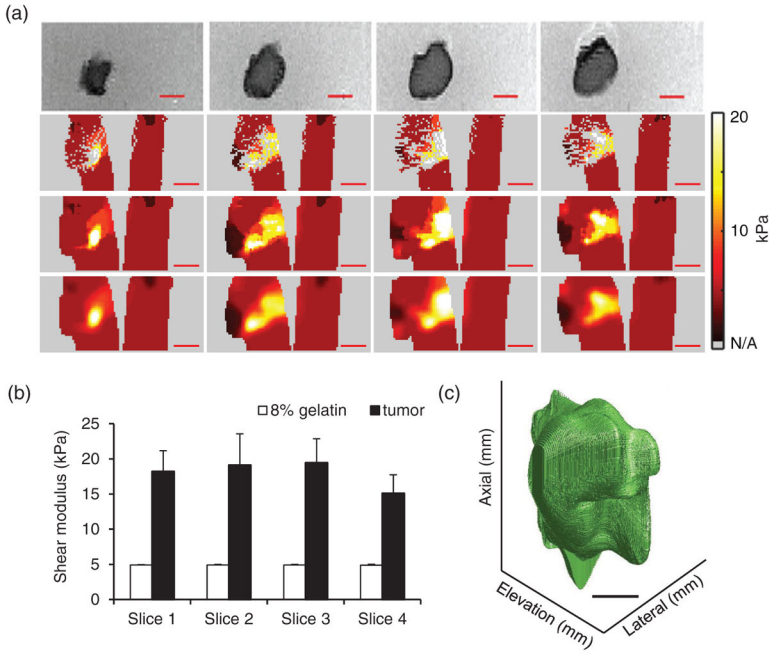

Figure 10.

3D reconstruction of NDL tumor inclusion. (a) Four slices of MR magnitude images (the first row) and the corresponding elasticity maps (the second row to the fourth row) showing the step-by-step processing as in figure 3. The interval distance between slices is 1 mm. The scale bars represent 5 mm. (b) The summarized shear moduli in gelatin and tumor inclusion. (c) The reconstructed 3D image based on the elasticity maps from (a). A 10 kPa threshold was chosen to detect the contour of the inclusion in each slice.

Table 1

Composition of the tissue-mimicking phantoms.

	Background material			Inclusion material		
Phantom	**Gelatin (wt/v %)**	**Agar (wt/v %)**	**Fiber (wt/v %)**	**Agar (wt/v %)**	**Fiber (wt/v %)**	**Others**
1	1.5	1.5	2	0	0	N/A
2	0	1	2	0	0	N/A
3	8	0	2	0	0	N/A
4	8	0	2	1	2	N/A
5	8	0	0	2	0	N/A
6	8	0	0	0	0	Neu deletion (NDL) tumor

Table 2

MRI acquisition parameters.

Repetition time (TR)/echo time (TE)/flip angle (FA) (ms/ms/°)	500/26.1/90
Refocusing angle (°)	180
MEG (mT m^{-1})	140
MEG duration (ms)	1
Field of view (mm^2)	80 × 80
Matrix size	240 × 240
Slice thickness (mm)	1
Spatially distinct slices	1
Number of excitation/averages	1
Bandwidth (kHz)	27
Slice repetitions	9

Table 3

Comparison of the shear modulus estimates of three tissue-mimicking phantoms obtained using the techniques of sst-MRE, US-SWEI and MT.

Phantom	sst-MRE Mean ± SD (kPa)	US-SWEI Mean ± SD (kPa)	MT Mean ± SD (kPa)
1	27.3 ± 2.3	28.2 ± 2.3	32.3 ± 1.8
2	10.6 ± 0.6	12.5 ± 2.1	10.1 ± 0.7
3	7.5 ± 0.3	7.9 ± 0.8	7.4 ± 0.5